Sensors & Diagnostics

PAPER

Check for updates

A highly stable room temperature titania nanostructure-based thin film transistor (TFT) alcohol sensor

Aditya Kumar Singh and Basanta Bhowmik [iD] *

The present study is concerned with the room temperature field-induced alcohol sensitivity of nanostructured TiO$_2$ thin films in field-effect transistor (TFT) configurations. The structural, morphological and optical characterizations of the TiO$_2$ thin film (grown *via* a low-cost solution process) revealed that the thickness of the film was ~220 nm with numerous pores on the surface. The average particle size was found to be 22 nm from XRD characterization. The surface roughness of the film was 215 nm. Photoluminescence studies showed that the TiO$_2$ band was 3.12 eV. The presence of oxygen vacancies and defect states was confirmed through PL spectroscopy and XPS studies. Electrical characteristics revealed a device mobility of ~13 cm^2 V^{-1} s^{-1}, I_{ON}/I_{OFF} ratio of ~2.16 × 10^4, subthreshold swing of ~31.4 mV dec^{-1} and threshold voltage of 0.65 V. The tuning of carrier concentrations at the sensing channel was achieved through gate biasing in the presence of vapor concentrations. At room temperature, exposure to ethanol, methanol and 2-propanol revealed a drastic drain current variation with shifts in the threshold voltage (V_{th}) for fixed V_{gs} and V_{ds}. The maximum alcohol response of the sensor in terms of drain current variation upon exposure to 100 ppm methanol, ethanol and 2-propanol were 71%, 60% and 51% at room temperature. Such drain current modulation and shifts in threshold voltage were correlated with carrier accumulation at the sensing channel, effects of near-surface bonds and polarization of gas molecules. The long-term stability and excellent alcohol sensing capability at room temperature will possibly pave way for the utilization of the sensor in low-temperature applications such as food storage and space application.

1. Introduction

Gas sensors have been of great significance in recent decades, following their huge applications in various sectors such as health care systems, automobiles, domestic security, consumer electronic systems and environmental monitoring systems.[1–3] There are many toxic gases emitted every day, which are hazardous to the environment and harmful to human health.[4] To avoid the toxic effects of these gases, there are tremendous demands for the development of room temperature-operated, low-cost, highly sensitive and selective gas sensors.[3,5,6]

Volatile organic compounds (VOCs) are commonly used in industries and laboratories and are easily evaporable, which leads to air pollution.[6] Their effects are more dominant in indoor spaces than outdoors. Alcohols are among the volatile and flammable organic compounds that are widely used as raw materials in medicine, organic synthesis, defense

industry and food industries.[1] Inhalation of alcohol vapors causes respiratory diseases, dryness, skin allergies, fatigue, central nervous system disorder and liver damage, which are serious hazards to human health.[1] Also, the detection of alcohol has many uses, for example, (i) to stop traffic fatalities caused by rush driving, (ii) a fast alarm against ethanol leakage in space aircraft and (iii) monitoring alcohol concentrations in beverages.[7] VOC contents are also present in the exhaled breath of patients suffering from diabetes, lung cancer, liver cancer, *etc.*, due to abnormal metabolism. Their detection acts as a biomarker for many diseases.[8]

In recent decades, semiconducting metal oxide (SMO) nanostructures have been widely studied for gas sensing. Their high compatibility for integration with microelectronic circuitry and high surface area with quantum confinement effects of nanostructured materials have made it possible to develop low-cost and portable devices for different applications.[10] The other influential factors of nanostructured SMOs such as abundant surface-active sites, fast electron transport kinetics, increased surface-to-volume ratio and lowest unoccupied molecule orbital (LUMO) energy provide beneficial advantages for their use as gas sensing materials.[11,12] Thus, tailoring nanostructured metal oxides is

Thin Film Device Laboratory, Department of Electronics and Communication Engineering, National Institute of Technology, Jamshedpur-831014, India. E-mail: bb.cemk.ece@gmail.com

---

important for achieving improved performance of gas sensing devices.[10] Various nanostructures of SMOs have been synthesized, such as zero-dimensional (0D) (*e.g.* nanoparticles), one-dimensional (1D) (*e.g.* nanowires and nanorods), two-dimensional (2D) (*e.g.* nanosheets) and three-dimensional (3D) (*e.g.* nanoflowers), for different applications.[11,13] Nanoparticles (OD) have attracted great attention from researchers in the gas sensing fields. They are easy to synthesize and offer a high surface area for maximum gas adsorption.[11] Therefore, to commercialize the semiconducting materials for gas sensing, it is necessary to optimize their morphology and microstructure.[12] Ajabshir *et al.* have reported the $Pr_2Ce_2O_7$ ceramic nanostructures synthesized *via* a chemical route, homogeneous sponge-like nanocrystalline praseodymium oxide (Pr_6O_{11}) synthesized *via* a facile precipitation route, nanostructured $Dy_2Sn_2O_7$–SnO_2 nanocomposites synthesized *via* a chemical route and zirconium dioxide (ZrO_2) nanoparticles prepared sonochemically. On the other hand, Derazkola *et al.* reported the neodymium oxide (Nd_2O_3) nanostructures synthesized by a solvent-less route for photocatalyst applications.[14–18]

The most preferred metal oxides for gas sensing were SnO_2, TiO_2, WO_3, ZnO, *etc.*, due to their batch fabrication, small dimensions, power consumption, higher stability and sensitivity towards many VOCs.[6,19,20] Titanium dioxide (TiO_2) has been actively studied in recent days for gas sensing due to its high chemical, mechanical and thermal stability,[2,20] its n-type semiconducting nature with a bandgap of 3–3.2 eV, and it exists in three phases, namely, rutile, anatase and brookite. Rutile is the most stable phase, whereas the anatase phase finds wide application in gas sensing.[11] The synthesis of various nanostructures of TiO_2 is possible through many simple techniques such as the solution process, electrochemical anodization, precipitation, hydrothermal and chemical vapor deposition.[11] However, the solution process method for nanostructured synthesis is easy, cost-effective and has precise control over the porosity distribution at oxide surfaces.[20,22,23] The oxygen vacancies and interstitial deficiencies present in these synthesized materials facilitate more sensitivity towards both reducing as well as oxidizing gases.[11,20,24] Several reports have shown the varieties of SMO materials synthesized *via* the chemical solution process for specific applications. For example, Asil *et al.* reported the $ZnCo_2O_4$/Co_3O_4 nanocomposite synthesis using Stevia extract (natural reagent) as a fuel in an auto-combustion sol–gel method.[25] Yang *et al.* reported the composite multi-walled carbon nanotubes (MWCNTs)-assembled $NiWO_4$ microflowers synthesized by a facile coprecipitation method, which exhibit excellent sensitivity towards NH_3.[26] Zonarsaghar *et al.* studied the synthesis of cerium vanadate ($CeVO_4$) nanoparticles through the chemical solution process.[27] Ajabshir *et al.* synthesized the nanostructures of $Ln_2Ce_2O_7$ (Ln = Er, Ho) ceramic through a sonochemical approach for toxic pollutants degradation under sunlight. Also, they reported the synthesis of an eco-friendly ceramic nanostructure of zinc cobalt oxide for the removal of organic contamination in the presence of sunlight.[28,29]

Metal oxide nanostructure-based resistive, metal–insulator–metal (MIM) and metal–insulator–semiconductor (MIS) sensor devices have been widely studied for the detection of alcohols (methanol, ethanol and 2-propanol).[7,30] However, conventional resistive or capacitive sensors are principally governed by the change in thin film resistance/dielectric constant in the presence and absence of gases.[7] Such channel resistance/conductance of the film is controlled by the density of carrier concentrations and their mobility.[31] The tuning of the carrier concentrations in resistive and capacitive devices has been achieved by employing the annihilation of the sensing surface to a certain level. The annihilation of the sensing material is required to supply necessary charge carriers for a reasonable conductance difference and to increase the analyte diffusion at the grain boundary by enhancing the activation energy.[20] The requirement of such temperatures implies greater power consumption, which necessitates battery-operated smart intelligent systems.[7] In such sensors, the operating temperature requirements are in the order of 200–500 °C for optimum sensing performance.[7,30] However, the real-time monitoring of the gases employing these sensors requires power in the order of a few milliwatts to several hundred milliwatts.[7,20,30,31] Because of the higher power consumption, it is difficult to integrate these sensors into monolithic integrated sensor platforms.[7]

Some previous studies on semiconducting metal oxide (SMO)-based resistive alcohol sensors have been investigated.[1,2,4–6,10,19,32–37] However, titanium dioxide-based three-terminal TFT alcohol sensors are rarely reported and are in their nascent stage. In this paper, Au/TiO_2 thin film/Ti-based thin film transistor gas sensors have been fabricated for the detection of alcohols at room temperature. Room temperature sensing performance by tuning the carrier concentrations in the sensing channel under different gate biases is the prime focus of the present paper. Gate biasing is used to direct access to the sensing channel by the gaseous molecules, which is found to have greater potential than the devices having a top-gated metal layer. Bias-controlled gas sensitivity of the nanostructured TiO_2 in field-effect configurations is highlighted and the corresponding gas sensing results have been correlated with the equivalent circuit model.

2. Experimental

All the chemicals were analytical grade and were used without further purification. TiO_2 thin film preparation was carried out by a low-cost solution process. In a typical process, 0.5 M $TiCl_4$ (titanium tetrachloride) (Sigma Aldrich, 99.9% pure) as the source of titanium was mixed with deionized water (H_2O) (resistivity 18 MΩ cm) (5% by volume) and allowed to stir (magnetic stirrer, 1 MLH, Remi Electrotechnik Ltd., India) at the rate of 300 rpm for 45 minutes at room temperature. Under stirring conditions, 100 ml of 0.1 M ethylene glycol was added dropwise to increase

the rate of reaction and cause the formation of TiO_2 to be faster. The mixture was then transferred to a flask maintained at the surrounding temperature of 0 °C.

The solution was aged for 72 hours. The *p*-Si wafer (thickness 380 μm, resistivity 8 Ω cm, <100>) used for film coating was initially cleaned in de-ionized water. After that, it was boiled in acetone for five minutes, then, rinsed with ethanol (Merck, 99.9%), followed by cleaning with concentrated HF solution and deionized water. The substrate was kept for drying in ambient air. A SiO_2 layer with a thickness of 110 nm was thermally induced on the cleaned *p*-Si substrate at ~1100 °C in O_2 and a humid environment. The SiO_2/Si substrate was dip-coated into the prepared solution for 30 s. After drying, the samples were annealed in an oven (Remco) at the increased temperature of 350 °C for 3 hours. A 50 nm thick Ti layer (as the back gate) was deposited at the back side of the Si substrate using an electron beam (EBEAM) evaporation system (12A4-D, Hind Hivac system, India). Similarly, Au was deposited on top of the TiO_2 layer to form a source and drain contact as shown in Fig. 1(a). Three samples were tested: one sample was tested immediately after fabrication (T1) and the other two were tested after aging for one month (T2) and two months

(T2), respectively, to verify the stability and repeatability of the device.

The crystallinity of the deposited TiO_2 thin film was studied using an X-ray diffractometer (model, Rigaku) with Cu Kα (λ = 0.1540 nm) radiation over a scanning range of 10–90° with a step of 0.02°. The chemical composition and the distribution of the synthesized material were analyzed using energy dispersive spectroscopy (EDAX, model: EAG AN461). The surface morphology of the thin film was investigated using the field emission scanning electron microscope (Zeiss, EHT = 5 kV). During the measurement, the sample was made conductive *via* a thin layer (Au) to have compatibility with the FESEM machine. The surface roughness analysis of the deposited film was done by atomic force microscopy (Model: Solver Pro, NT-MDT) in non-contact mode. The AFM image was analyzed *via* Scanning Probe Image Processor software (SPIP 6.0.14). The bandgap and OVs of the sample were studied through a photoluminescence (PL) study using a Horiba Jobin Yvon, Flurolog-3 spectrofluorometer (model FL3-22) at room temperature. The authentication of OVs-induced defects was further confirmed by X-ray photoelectron spectroscopy (XPS) (PHI-5400, Perkin-Elmer Com.).
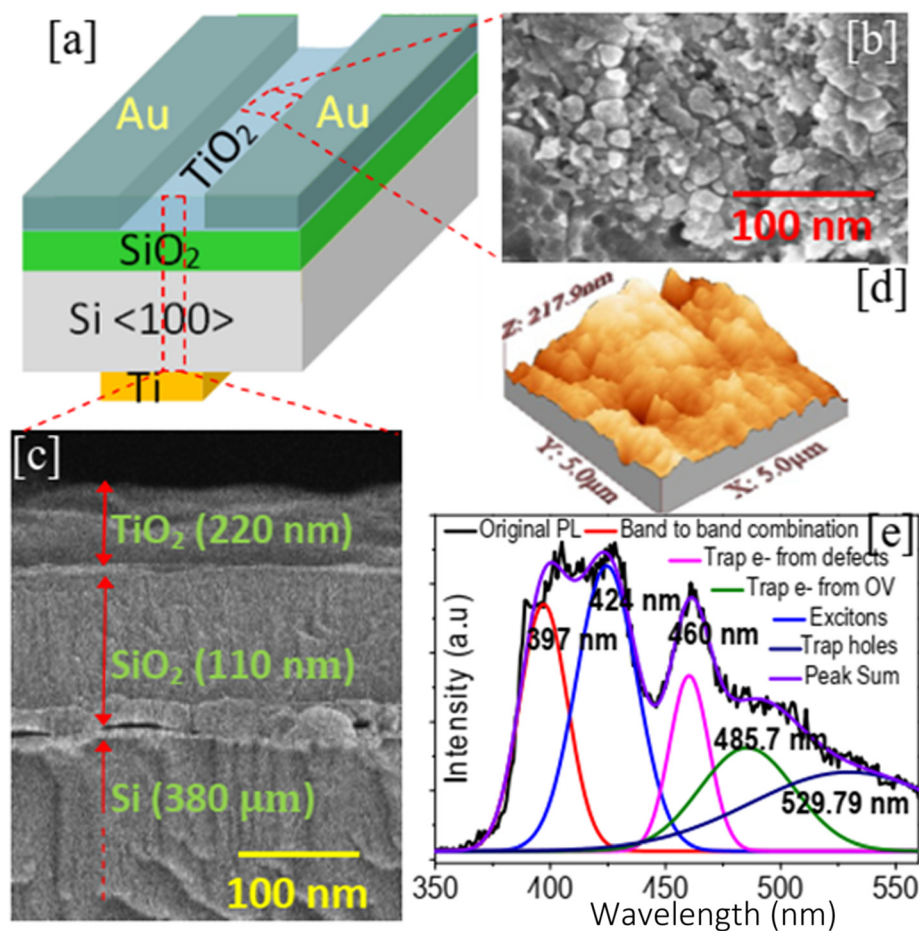

Fig. 1 (a) Schematic of the device structure, (b) surface morphology of the deposited TiO_2 thin film, (c) cross-sectional FESEM of the device structure, (d) TiO_2 surface study through AFM, and (e) PL spectra of the as-prepared TiO_2 film.

The electrical and sensing characterizations of the fabricated sensor device were carried out in a cylindrical dynamic flow chamber similar to that reported in ref. 31. Two air cylinders were used, one for carrier gas and another for bubbling the VOCs. The airflow rate of the cylinder was controlled by a mass flow meter (MFM, BMF-4000, India). A temperature controller was used to maintain the temperature inside the cylindrical dynamic flow system. The Keithley 6487 picoammeter was used to measure the variation in resistance/current and the data were collected manually. The sensor response magnitude was given by RM (%) = $[(I_g - I_o)/I_o] \times 100\%$. Here, I_0 is the drain current in air and I_g drain in the test gas.[34] The response time of the device was the time required to achieve 90% of the maximum response. The recovery time was the time required to fall to 90% of the maximum saturated value.

3. Results and discussion

3.1. Structural characterizations

Fig. 1(b) and (c) depict the surface and cross-sectional FESEM image of the TiO$_2$ thin films. As elucidated from Fig. 1(b), the surface of the thin film has a particle-like structure with a size of 10–25 nm. The thin film surface was porous and the porosity was recorded to be 51–56%. Cross-sectional FESEM suggested that the thickness of the deposited film was ~220 nm. The deposited film was crack-free but uneven throughout the entire surface. This was possibly due to the annealing of the sample at 350 ° C. The growth of TiO$_2$

nanoparticles occurs following the formation of small nuclei in the liquid. The small nuclei then grow as atoms. Initially, hydrolysis of titanium chloride (TiCl$_4$) occurs in deionized water (H$_2$O) to form unstable titanium hydroxide Ti(OH)$_4$.[20] The titanium hydroxide after polycondensation decomposes to form suspended titanium dioxide (TiO$_2$) nuclei. The addition of ethylene glycol increases the condensation process and thus the formation of TiO$_2$ becomes faster. The nuclei aggregate at the substrate to grow as nanoparticles.

$$TiCl_4 + H_2O \rightarrow Ti(OH)_4 + HCl \quad (1)$$

$$2Ti(OH)_4 \rightarrow TiO_2 + H_2O \quad (2)$$
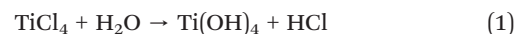
The AFM study of the deposited TiO$_2$ thin film was carried out for the scanning area of 5 μm × 5 μm as shown in Fig. 1(d). Surface roughness of ~218 nm, roughness peak-to-peak value of ~360 nm, average roughness of ~215 nm and an average height of ~202 nm were determined. Such high roughness is good for gas-sensing applications.[11] EDS analysis (shown in Fig. 2(a)) was carried out to obtain the weight percentage of Ti and O in TiO$_2$ film. The weight percentage of Ti and O were found to be 44.68% and 55.32%, respectively. No other peaks were observed, which confirmed the formation of TiO$_2$ with high purity.

Further, XRD analysis (not shown), confirmed the anatase crystalline formation of TiO$_2$ with dominant {101} and {004} reactive crystalline facets. The sharp peak belongs to the anatase TiO$_2$ crystalline phase and agrees well with the
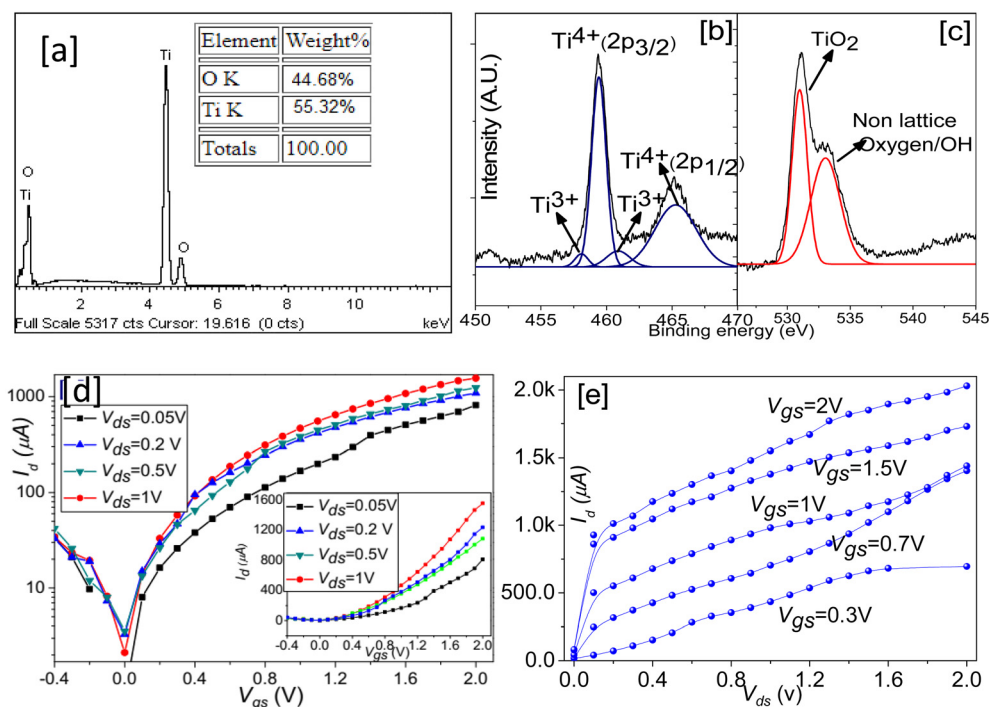

Fig. 2 (a) EDS analysis of the as-prepared TiO$_2$ thin film. (b) and (c) XPS spectra of TiO$_2$ (b) showing the deconvolution spectrum of Ti 2p$_{3/2}$ and Ti 2p$_{1/2}$, and (c) the O1S spectrum. (d) I_d as a function V_{gs} (−0.4–2 V) for the V_{ds} of 50 mV, 200 mV, 500 mV and 1 V (the inset shows the same graph in linear scale) and (e) I_d as a function of V_{ds} for different V_{gs}.

standard JCPDS file no. 21-1272.[38] The peaks (101) and (004) were at 25.32° and 36.02°, respectively. The crystal size was calculated using the well-known Scherrer's formula $D = 0.9\lambda/\beta\cos 2\theta$,[39–40] where λ is the wavelength of X-rays, θ is the angle of incidence and β is the full width at half maximum. The average crystallite size was calculated to be in the range of 20–22 nm. The absence of any other peaks in the XRD pattern indicated that the deposited TiO_2 thin film was undoped and pure.

A room temperature photoluminescence (PL) study was conducted in the wavelength ranging from 350–560 nm for the excitation wavelength of 325 nm (shown in Fig. 1(e)). Lorentzian fitting of the PL spectra demonstrated five emission peaks in the spectral range of 350–560 nm. the emission peak at 397 nm corresponds to band-to-band recombination (red line), which ensured the bandgap of TiO_2 as 3.12 eV. The peak at the lower energy side, 424 nm (blue line), attributed to excitons suggested the presence of surface oxygen vacancies and at the lower energy side, two other peaks at 460 nm and 485.7 nm indicate the existence of defect states.[21] Peaks at relatively higher wavelengths 529.79 nm were attributed to the recombination of electrons and hole trap states above the valence band.[21]

X-ray photoelectron spectra of the grown TiO_2 thin film are shown in Fig. 2(b and c). Ti (2p) photoelectron spectra depict the formation of different sub-oxide states of the TiO_2, such as TiO, Ti_2O_3, etc.[41] The sub-oxides were probably formed due to oxygen vacancy (OV) variations in the synthesized material because of the limited content of water in the electrolytes.[20] The peaks at 530 nm and 532.3 nm were assigned to the lattice oxygen (Ti–O), of TiO_2 and surface oxygen (non-lattice oxygen).[41,42] The surface oxygen resulted from the adsorbed oxygen ions (air) or adsorbed hydroxyl ions (water) at the thin film surface.

3.2. Electrical characterization

Before investigating the field-induced gas sensitivity of the device, room temperature electrical characterizations were carried out for various V_{gs} and V_{ds} as shown in Fig. 2(c) and (d). A negative potential causes electron depletion at the sensing channel, whereas a positive potential leads to electron enhancement, which suggests that the device behaves similarly to the n-channel enhancement type FET.[32] From the current–voltage characteristics (Fig. 2(d)), the measured threshold voltage (V_{th}) upon extrapolation of the linear region was found to be 0.65 V in ambient air. The calculated I_{ON}/I_{OFF} ratio and subthreshold swing (SS) were 2.16×10^4 and 31.4 mV/dec, respectively for the V_{ds} of 1 V. Electron mobility, determined using the formula $\mu = (\delta I_d)/(\delta V_{gs})(L/(WC_{ox}(V_{gs} - V_t)))$, was 13 cm² V⁻¹ s⁻¹.[43] Contact resistance (R_c) was calculated considering the Y intersection (extrapolating up to $V_{gs} - V_t = 0$ V) of the plot R_{ds} vs. $1/(V_{gs} - V_t)$ (not shown) and was found to be ~600 kΩ, whereas the channel resistance was ~1.49 MΩ. In the n-type TiO_2 channel for $V_{gs} < 0$ V, no charge accumulation occurred, as elucidated

by the order of the OFF current (~720 nA). However, in the voltage range $0 < V_{gs} < V_t$ (0.65 V), a small amount of drain current (I_{ds}) was observed as evidenced by the subthreshold swing rate ~31.4 mv dec⁻¹. The value of the subthreshold swing suggests negligible leakage current and hence low power consumption in ideal conditions. At a higher gate-to-source voltage ($V_{gs} > 0.65$ V), a positive gate bias induces an accumulation of electron layer at the SiO_2/TiO_2 interfaces and hence at the sensing channel.[35] Such phenomena ensure the switching of the drain current (I_{ds}) from the OFF state (depletion of electrons) to the ON state (accumulation of electrons) shown in the inset of Fig. 2(d). The application of varying V_{ds} ensured a further increase in drain current (I_{ds}) as reflected in Fig. 2(e). Fig. 2(d) demonstrates a linear increment in current (I_{ds}) up to the drain-source voltage (V_{ds}) of 0.2 V and beyond that saturation tendency. The drain current (I_{ds}) was found to be a function of both V_{ds} and V_{gs} in the voltage ranging from 0–0.2 V, whereas, in the saturated region (>0.2 V), the modulation of drain current ((I_{ds})) was only pronounced with the variation in gate voltage (V_{gs}).

4. Sensor study

Alcohol vapor was tested at room temperature for the drain-source voltage of 1 V and $V_{gs} = 0$ V, 1.15 V, 1.65 V and 2.15 V, respectively. Fig. 3(a) shows the drain current (I_d) fluctuation at different alcohol concentrations (1–100 ppm) for the fixed $V_{gs} = 1$ V and $V_{ds} = 1$ V. The drain current (I_d) was found to increase when exposed to alcohols and decrease after the exposure was cut off. The results were found to be reproducible for several cycles of switching the vapor pulse ON and OFF (not shown). However, the response magnitude $[(\Delta I/I_o) \times 100]$ order was methanol (71%) > ethanol (60%) > 2-propanol (51%) at 100 ppm concentrations (Fig. 3(a)). The threshold voltages (V_{th}) were found to be shifted at 0.5 V, 0.42 V and 0.4 V for the exposure of 100 ppm of 2-propanol, ethanol and methanol, respectively, with reference to that of air (0.65 V). Fig. 3(b) shows the comparative drain current fluctuation among 100 ppm of methanol, ethanol and 2-propanol for the variation of $V_{gs} = 0$ V, $V_{gs} - V_t = 0.5$ V, $V_{gs} - V_t = 1$ V and $V_{gs} - V_t = 1.5$ V. As can be seen from the graph (Fig. 3(b)), the drain current increases with the increase in gate voltage for all VOCs. Such an increase in drain current can be attributed to the positive gate-induced vertical electric field, which modifies the depletion region (and hence carrier concentration profile) at the TiO_2 channel. Further, the vertical electric field accelerated the release of surface-trapped carriers by charge exchange between the TiO_2 sensing channel and alcohol molecules, resulting in a shift in the Fermi energy level.[9] A comparison of the alcohol sensing performances of different TFT sensors is tabulated in Table 1. Wongrat et al. reported the ZnO nanostructure-based field effect transistor (FET) sensor for ethanol sensing at room temperature and compared it with the ZnO thin film FET sensor. On exposure to ethanol vapors (100 ppm), the response of the ZnO nanostructure-based FET sensor was
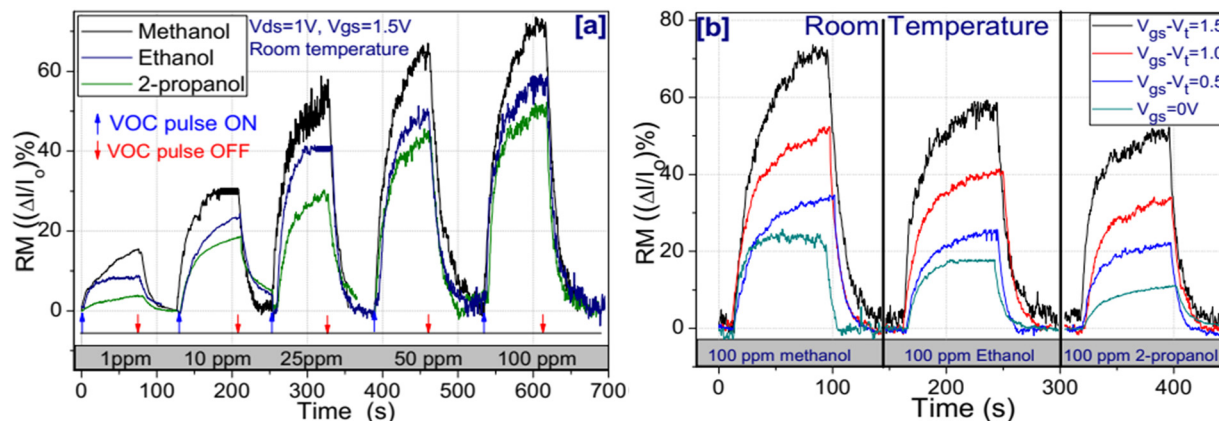
Fig. 3 (a) Room temperature transient response to methanol, ethanol and 2-propanol at V_{ds} = 1 V, V_{gs} = 1.5 V; (b) room temperature transient response to methanol, ethanol and 2-propanol for $V_{gs} - V_t$ of 0 V, 0.5 V, 1 V and 1.5 V.

Table 1 Comparison of alcohol sensors based on a TiO$_2$ thin film sensing layer

Sl. No	Material	Vapor	Dynamic range	RM (%)	Res time (s)	Rec time (s)	Ref.
1	Yb-doped In$_2$O$_3$	Ethanol	1–50 ppm	40	180	260	1
2	PANI/TiO$_2$	Ethanol	5–20 ppm	NA	115	340	2
3	P3HT-based OFETs	Ethanol	0–3000 ppm	2.6	480	NA	4
4	LaFeO$_3$	Ethanol	10–1000 ppm	12.5	9	72	5
5	ZnO/OV-225	Ethanol	1400 ppm	59	420	1740	6
6	In$_2$O$_3$	Ethanol	5–100 ppm	21.1	50–60	50–60	10
7	ZnO	Ethanol	100 ppm	3	NA	NA	19
8	ZnO nanostructure	Ethanol	50–100 ppm	26.9	32.5	29	32
9	ZnSnO	IPA	NA	69.4	74.6	205	33
10	CuPc and pentacene	Ethanol	0–100 ppm	70	236.8	197.4	34
11	Graphene FET array	Ethanol	NA	17.4	NA	NA	35
12	Al-doped-ZnO	Methanol	100–500 ppm	44	123	125	36
13	Poly-DPOT	1-Hexanol	700–1500 ppm	0.32	60	75	37
14	TiO$_2$	Methanol	1–100 ppm	71	50.7	40.0	Present work
		Ethanol	1–100 ppm	60	51.2	41.8	
		2-Propanol	1–100 ppm	51	60.0	43.3	

RM (%) = response magnitude, res time (s) = response time, rec time (s) = recovery time, NA = not available.

found to be 6, whereas the ZnO thin film FET sensor response was 3. The sensitivity improvement of the device at room temperature can be attributed to the increase in the surface-to-volume ratio of nanostructures.[32] Jun *et al.* showed improvement in the ethanol sensing performance employing Yb doped in In$_2$O$_3$. The 4 mol% of the Yb-doped In$_2$O$_3$ nanofiber FET sensor fabricated *via* the electrospinning process exhibited an optimum response towards ethanol.[1] Ponhan *et al.* reported the ZnO nanostructure-based TFT ethanol sensor. The ZnO thin film was deposited over a *p*-Si substrate by a thermal evaporation process. The device showed good sensitivity towards ethanol at room temperature with negative gate bias modulation.[19] Seetha *et al.* studied the room temperature sensing of ethanol vapors *via* an indium oxide-based FET sensor. The thin film of porous indium oxide was treated with a dip coating technique. The device was tested with ethanol, acetone and ammonia gas and was found to be most selective towards ethanol vapor. The reason for the high selectivity was attributed to the ethanol functional group and moisture. Zhao *et al.* studied

the perovskite composite oxide of a LaFeO$_3$ nano-crystalline thin-film synthesized through a sol–gel process for the detection of ethanol gas. It was found that the device recovery performance was improved by 38% *via* the doping of LaFeO$_3$ with strontium. The La$_{0.7}$Sr$_{0.3}$FeO$_3$ sensor showed good sensitivity, excellent selectivity, and good stability toward ethanol. It exhibited better anti-disturbance properties toward other gases such as gasoline, carbonyl, isobutane and sulphuretted hydrogen.[5] Dutta *et al.* reported a thin film of zinc tin oxide (ZTO) deposited through a solution process for the detection of isopropyl alcohol (IPA) at room temperature. Their TFT sensor device performance was optimized *via* the post-annealing temperature. The device annealed in the temperature range of 400–500 °C exhibited better sensing performance in terms of stability, long lifetime, fast response time and high sensitivity as compared to the device annealed at 600 °C. This was possibly due to the formation of a higher diameter grain size and the diminishing of the surface defects upon post-annealing at 600 °C.[33] Lee *et al.* reported a pentacene-deposited copper phthalocyanine (CuPc) organic

thin film transistor for ethanol vapor detection. It was found that a 5 nm thick layer of copper phthalocyanine (CuPc) deposited over a 50 nm thick pentacene layer exhibited excellent sensitivity towards ethanol vapor at room temperature. The device was more selective towards ethanol than other gases such as O_2, NO_2 and N_2.[34] Lienerth et al. reported the P3HT-based OFETs for the sensing of polar VOCs by monitoring both the charge carrier mobility and drain current at fixed gate voltage. In their study, the hysteresis of the transfer curve was used as an additional parameter for the detection of target gases. They suggested that one can improve the VOC selectivity if the hysteresis can be combined with the on-current or mobility of the device.[4] Chen et al. demonstrated the graphene FETs arrays on microchannels for ethanol gas detection. Narrow walls of SU-8 (a negative photoresist) were deposited on the substrate having top metal electrodes. It was then pressed with the predeposited graphene Si/SiO_2 substrate making contact with the metal electrodes acting as the source and drain. The optimum response of the device was found to be 17.4% upon exposure to ethanol and was very well recovered when the gas supply was cut off.[35] Jang et al. studied the siloxane polymer-coated ZnO thin film for ethanol gas sensing. The sensitivity of the device towards ethanol was three times greater with respect to pristine ZnO at room temperature. The improved sensitivity was due to intermolecular interactions of gas-selective polymers with gas molecules.[6] Gawri et al. reported the nanocomposite material of polyaniline/titanium dioxide ($PANI/TiO_2$) as well as pristine titanium dioxide (TiO_2) for ethanol gas sensing at room temperature. The optimum response of the $PANI/TiO_2$-based sensor towards 20 ppm ethanol was found to be 47. The response time/recovery time was found to be 115 s and 340 s, respectively. The $PANI/TiO_2$ showed a better sensing response than pristine TiO_2 nanoparticles.[2] Sahay et al. demonstrated that the Al-doped ZnO thin film was deposited via a chemical spray pyrolysis technique over a glass substrate for methanol detection. It was found that the 0.5 at% Al-doped ZnO film showed the optimum response of ~44% towards 500 ppm of methanol vapors at 275 °C. The response time/recovery time was found to be 123 s and 125 s, respectively. The improved response of the Al-doped ZnO thin film over undoped ZnO was attributed to the combined effects of small crystallite size as well the low lattice disorder of the film.[36] Torsi et al. reported the dipentoxy-substituted polyterthiophene (Poly-DPOT)-based organic thin film transistor for the alcohol sensor. The device responses to ethanol and 1-hexanol molecules were reversible and fast. Optimum sensitivities were recorded to be 0.7 ng ppm^{-1}.[37] As evident from the table and comparative discussion, most of the studies reported ethanol sensors. The simultaneous study of ethanol, methanol and 2-propanol is rarely reported at room temperature. The present sensor showed very good long-term stability with a considerably higher response magnitude and was more selective towards methanol among the alcohols from the same alcohol group.
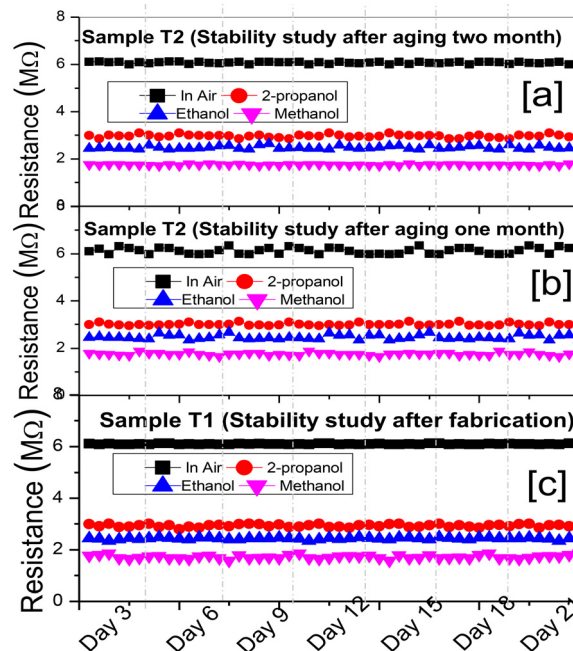

Fig. 4 Stability study in air, 100 ppm of methanol, ethanol and 2-propanol for the sample (a) T1 (no aging), (b) T2 (one month of aging after fabrication), and (c) T3 (two months of aging after fabrication).

Stability studies were conducted for three samples, viz., T1–T3 in air, methanol, ethanol and 2-propanol at room temperature for seven days as shown in Fig. 4. The baseline resistance in air was found to be constant with a variation of ±1.7%, whereas for methanol, ethanol and 2-propanol it was ±2.17%, ±1.9% and ±2.3%, respectively, for all the samples. However, the stability fluctuation among the three samples was ±0.9%. The repeatability of the device (not shown) was tested for three samples (T1–T3) under similar measurement conditions. All three samples showed fully reversible characteristics after the VOC exposure was OFF. However, small deviations in sensor parameters, viz., sensor response, response time and recovery time, were found to be ±0.96%, ±2.58% and ±1.87%, respectively. Such small deviations were possibly due to the carrier concentration differences during the growth of the TiO_2 thin film using the solution process.

The effect of relative humidity (RH) on the device sensing performance was investigated at room temperature under 65% RH and 90% RH. The device was exposed to 100 ppm of the alcohols in combination with 65% RH and 90% RH for the V_{ds} of 1 V and V_{gs} of 1.5 V. The device responses towards 100 ppm of methanol, ethanol and 2-propanol in combination with 65% RH were found to be 73%, 62.4% and 54%, respectively. Whereas, towards 100 ppm of methanol, ethanol and 2-propanol mixed with 90% RH, the responses were 73.2%, 62.7% and 55.5%, respectively. It is worth mentioning at lower relative humidity (65% RH), the variation in sensor response was possibly due to the adsorption of water molecules on the TiO_2 surfaces, and the subsequent dissociation of the same at the active site possibly helps to accumulate dipoles (OH^-) and mobile

protons (H$^+$). The formation of such dipole (hydroxyl ions) and mobile protons increases the electron concentrations in the TiO$_2$ layer. This process decreases the depletion width (λ_d), which thereby reduces the sensor baseline resistance.[44] The deviation in response magnitude under relative humidity with respect to dry air was found to be ±8.82%. Further, we also studied the alcohol sensitivity of the present device at higher temperatures to observe the maximum achievable sensor response. The maximum sensor responses of 86%, 79% and 74% towards methanol, ethanol and 2-propanol were obtained at 250 °C.

Selectivity is the prominent parameter to determine the sensing capabilities of the device. To investigate the selectivity, the sensor device was exposed to 100 ppm of methanol, ethanol, 2-propanol, acetone, benzene, toluene and xylene at room temperature. As revealed in Fig. 5, the device showed the maximum response towards methanol among the tested gases. The responses of the device towards methanol, ethanol, 2-propanol, acetone, benzene, toluene and xylene were found to be 71%, 60%, 51%, 23%, 20%, 16% and 13%, respectively. The higher selectivity towards methanol was probably attributed to the lower molecular weight and lower carbon chain length, which facilitate the easy binding with the TiO$_2$ thin film.[45] The polarity of the alcohols decreases as the carbon chain length increases. Also, with increasing molecular size, it might not be easy to reach the active sites of the nanostructured thin film but methanol can easily bind to their surface due to the smaller molecular size and greater polarity than ethanol as well as 2-propanol. These two effects indicate a greater sensitivity towards methanol.[45]

5. The role of surface states in the sensing mechanism

The positive potential above the threshold voltage forms strong conduction channels through the accumulation of majority charge carriers near the oxide and TiO$_2$ interfaces.[32] Such a gate potential is possibly the reason for charge carrier

Fig. 5 Selectivity study on the TiO$_2$ thin film-based TFT gas sensor at room temperature.

separation at the semiconducting layer. The TFT structure and its equivalent capacitance model, energy band diagram and electron flow mechanism are pictorially shown in Fig. 6(a)–(f). The chemisorption of air with subsequent carrier exchange is shown in Fig. 6(a), and the same is shown in Fig. 6(b) for methanol exposure. Fig. 6(c) shows that energy bands are flat in ideal conditions, *i.e.* for V_{gs} = 0 V. Fig. 6(d) reveals (when $V_{gs} > V_{th}$) electron accumulation at the SiO$_2$–TiO$_2$ interface, which causes bands to bend downwards. It is worth noting that in Fig. 6(d), band bending is more effective in methanol exposure (solid line) than that in air (dotted line). Such a phenomenon is attributed to the following: (i) as $V_{GS} > V_{th}$, the accumulation of delocalized electrons near the SiO$_2$–TiO$_2$ interface helps to form channels. (ii) The number of carriers from such channels decrease (keeping $V_{GS} > V_{th}$) when the device is exposed to air. In air, physisorbed O$_2$ is converted to O$^-$, O^{2-} and O$_2^-$ by accepting channel electrons, resulting in downward band bending and an increase in channel resistivity. (iii) However, upon methanol exposure and subsequent oxidation, trapped electrons are released back into the sensing channel. The release of trapped carriers increases the total number of free carriers at the sensing channel and hence increases the conductivity of TiO$_2$. In such conditions, the positive potential at the drain terminal ($V_{DS} > 0$) causes electron injection from the source towards the drain, leading to the current conduction. Therefore, the drain current can be modulated by either changing the gate potential or increasing the test gas concentrations. One can increase V_{gs} up to a certain limit (in the present case 2 V); beyond that, the device enters the linear region. Further, a higher gate potential will provide the maximum drain current but at the cost of a similar heating problem to that encountered in resistive devices. On the other hand, drain current enhancement with the increase in gas concentration also has a certain limit as the gas adsorption and subsequent oxidation are surface-limited reaction mechanisms In the present study, 100 ppm is the optimum alcohol concentration for TiO$_2$ surfaces; beyond that, the increase in adsorption scattering and the lower gas sticking coefficient (θ) cause surface saturation, leading to the constant drain current. In a nutshell, channel charge density is governed by accumulated sheet charge density, which is non-uniform throughout the channel and solely depends on the applied gate potential and amount of gas exposure. As evident in Fig. 6(a) and (b), the sensing mechanism of the present TFT device is governed by the amount of alcohol adsorption–desorption and subsequent charge transfer between the TiO$_2$ sensing layer and alcohol molecules. The already chemisorbed surface O$^-$ reacts with alcohol molecules and produces hydrocarbon byproducts and releases surface-trapped electrons according to eqn (3). The number of released trapped electrons (shown in eqn (4)) and hence current conductivity depend on the reaction rate co-efficient (k). The release of trapped carriers will continue until an equilibrium Fermi energy is reached within the adsorption–desorption system. The sensor response formula,
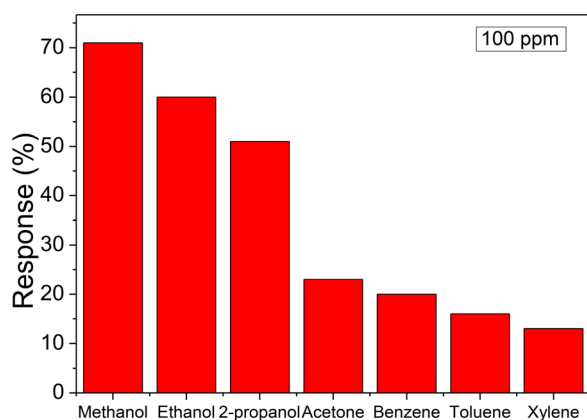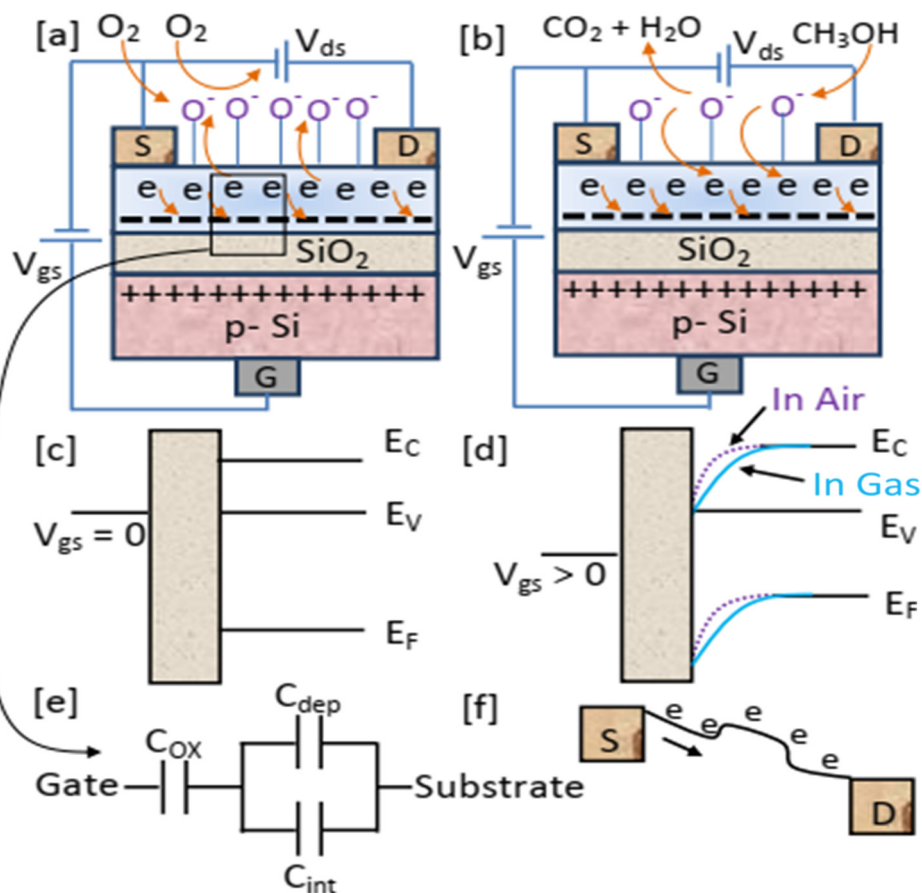
Fig. 6 A schematic of the device structure with charge transfer processes (a) in air, and (b) in gases; (c) energy band diagram in ideal flat conditions *i.e.* for $V_{gs} = 0$ V; (d) the corresponding energy band alignment in air and gases; (e) the capacitance model at the SiO_2–TiO_2 interface and (f) the carrier transport mechanism.

correlating with the number of released trapped carriers (n), available surface sites (O^-) and reaction rate co-efficient k_{gas}, is shown in eqn (5),[13] where T = test alcohol molecules, m = constant, n = number of surface trapped electrons, T' = oxidation byproducts (CO_2, CO, H_2O), n_a = number electrons in air and n = number electrons in alcohols.

$$T(\text{gas}) + 5O_{ads}^m \rightarrow T' + ne^- \tag{3}$$
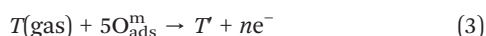
$$dn/dt = k_{gas}[O_{ads}]^m[T]^m \tag{4}$$

$$RM = \{\Gamma_t k_{gas}[O^-_{ads}]^m[T]^m\}/n_g \tag{5}$$

Carrier transport in the TFT structure is correlated through surface state modelling (shown in 6 (a and b) and Fig. 6(f)). The surface state depends on the gas concentrations as well as the sweep rate of the gate voltage, which modulate the transfer characteristics of the TFT devices.[3] Carrier trapping is dominant in ambient air with higher sweep rates.[3,46,47] On the other hand, the detrapping of the same occurs through charge transfer from the surface to the sensing channel. Such a charge transfer process (due to surface interaction with target gases) causes strong accumulation at the sensing channel. The energy band diagram in Fig. 6(d) shows carrier

trapping (dotted line) and detrapping (solid line) phenomena. For $V_{GS} < V_{th}$ (OFF state), the positive charge at the SiO_2–TiO_2 interface forms a depletion region and the width of the region decreases for $V_{GS} > V_{th}$ (as the field penetrates deeper into the channel).[48] An equivalent capacitance model (Fig. 6(e)) demonstrated the parallel connection of C_{int} (interface state capacitance) and C_{acc} (intrinsic accumulation capacitance) in series with TFT oxide capacitance (C_{OX}).[48] The gate capacitance (C_{OX}) decreases with the increase in surface reaction or carrier detrapping phenomena and for the same reason, the interface state capacitance increases.[47,48] The interface capacitance C_{int} = $(dQ_{int})/(d\Psi_S) = q(dn_{int})/(dE_S)$ F/cm^2 (E_S = energy at SiO_2–TiO_2 interface, Ψ_S = surface potential, n_{int} = surface state density, Q_{int} = charge density in the gate area,) is the governing factor for creating surface bands leading to the conduction of current.[47]

6. Conclusion

Room temperature TiO_2 thin film in the TFT configuration for alcohol sensing is presented in this paper. The chemically synthesized TiO_2 thin film showed numerous pores with uneven surfaces having oxygen vacancies originating from

the paucity of water in the eletrolytes. Electrical characteristics suggest the n-channel enhancement-type FET characteristics of the fabricated device as confirmed through the threshold voltage shifts towards the lower V_{gs} regime. The threshold voltage (V_{th}) was found to be 0.65 V in air and upon exposure to 100 ppm of methanol, ethanol and 2-propanol, it was shifted to 0.4 V, 0.42 V and 0.5 V, respectively. The other properties such as I_{on}/I_{off} (10^3) and sub-threshold swing (3.14 mV/decade) in air indicated negligible leakage current in the device. It is worth mentioning that the drain current (I_d) change was optimum for the simultaneous excitation of the gate sweep voltage and exposure to VOCs. Such drain current fluctuation is correlated with the carrier trapping-detrapping phenomena and carrier density at the sensing channel. However, the device was found to be more sensitive to methanol among the tested gases and their response magnitudes were in the order of methanol (71%) > ethanol (60%) > 2-propanol (51%) at 100 ppm concentration. In addition, the minimum response variation under a humid environment, and better long-term stability with room temperature alcohol sensing capability of the present device pave the way for the application of the sensor in harsh environments.

Author contributions

Both authors equally contributed.

Conflicts of interest

There are no conflicts to declare.

Acknowledgements

References

1 L. Jun, Q. Chen, W. Fu, Y. Yang, W. Zhu and J. Zhang, *ACS Appl. Mater. Interfaces*, 2020, **12**, 38425–38434.

2 I. Gawri, R. Ridhi, K. P. Singh and S. K. Tripathi, *Mater. Res. Express*, 2018, **5**, 025303–025326.

3 H. S. Jeong, M. J. Park, S. H. Kwon, H. J. Joo and H. I. Kwon, *Sens. Actuators, B*, 2019, **288**, 625–633.

4 P. Lienerth, S. Fall, P. Lévêque, U. Soysal and T. Heiser, *Sens. Actuators, B*, 2016, **225**, 90–95.

5 S. Zhao, K. O. S. Johnny, B. Xu, M. Zhao, Z. Peng and H. Cai, *Sens. Actuators, B*, 2000, **64**, 83–87.

6 M. Jang, J. Lee, S. Y. Park, J. Lee, K. M. Lee, W. Song, S. Myung, S. S. Lee, H. K. Jung, Y. C. Kang, S. K. Kwak and K. S. An, *Appl. Surf. Sci.*, 2021, **542**, 148704.

7 J. K. Abraham, B. Philip, A. Witchurch, V. K. Varadan and C. C. Reddy, *Smart Mater. Struct.*, 2004, **13**, 1045–1049.

8 B. Liu, A. Libanori, Y. Zhou, X. Xiao, G. Xie, X. Zhao, Y. Su, S. Wang, Z. Yuan, Z. Duan, J. Liang, Y. Jiang, H. Tai and J. Chen, *ACS Appl. Mater. Interfaces*, 2022, **14**, 7301–7310.

9 Md. A. H. Khan, R. Debnath, A. Motayed and M. V. Rao, *Sensors*, 2021, **21**, 624–630.

10 M. Seetha and D. Mangalaraj, *Appl. Phys. A: Mater. Sci. Process.*, 2012, **106**, 137–143.

11 X. Tian, X. Cui, T. Lai, J. Ren, Z. Yang, M. Xiao, B. Wang, X. Xiao and Y. Wang, *Nano Mater. Sci.*, 2021, **3**, 390–403.

12 K. Shingange, H. C. Swart and G. H. Mhlongo, *Sens. Actuators, B*, 2020, **308**, 127670–127681.

13 B. Bhowmik and P. Bhattacharyya, *RSC Adv.*, 2015, **5**, 82159–82168.

14 S. Z. Ajabshir, E. Shafaati and A. Bahrami, *Ceram. Int.*, 2022, **48**, 24695–24705.

15 S. Z. Ajabshir, M. S. Morassaei and M. S. Niasari, *J. Colloid Interface Sci.*, 2017, **497**, 298–308.

16 S. Z. Ajabshir and M. S. Niasari, *J. Mol. Liq.*, 2016, **216**, 545–551.

17 S. Z. Ajabshir and M. S. Niasari, *New J. Chem.*, 2015, **39**, 3948–3955.

18 S. M. Derazkola, S. Z. Ajabshir and M. S. Niasari, *J. Mater. Sci.: Mater. Electron.*, 2015, **26**, 5658–5667.

19 W. Ponhan, S. Phadungdhitidhada and S. Choopun, *Mater. Today: Proc.*, 2017, **4**, 6342–6348.

20 B. Bhowmik, *J. Electron. Mater.*, 2019, **48**, 7292–7301.

21 A. Saha, A. Moya, A. Kahnt, D. Iglesias, S. Marchesan, R. Wannemacher, M. Prato, J. J. Vilatela and D. M. Guldi, *Nanoscale*, 2017, **9**, 7911–7921.

22 Y. Su, G. Chen, C. Chen, Q. Gong, G. Xie, M. Yao, H. Tai, Y. Jiang and J. Chen, *Adv. Mater.*, 2021, 2101262–2101283.

23 Y. Su, W. Li, L. Yuan, C. Chen, H. Pan, G. Xie, G. Conta, S. Ferrier, X. Zhao, G. Chen, H. Tai, Y. Jiang and J. Chen, *Nano Energy*, 2021, **89**, 106321–106329.

24 C. Chen, M. Jiang, X. Luo, H. Tai, Y. Jiang, M. Yang, G. Xie and Y. Su, *Sens. Actuators, B*, 2022, **370**, 132441–132448.

25 S. A. H. Asil, S. Z. Ajabshir, H. A. Alshamsi, A. A. Nayili, Q. A. Yousif and M. S. Niasari, *Int. J. Hydrogen Energy*, 2022, **47**, 16852–16861.

26 M. Yang, C. Au, G. Deng, S. Mathur, Q. Huang, X. Luo, G. Xie, H. Tai, Y. Jiang, C. Chen, Z. Cui, X. Liu, C. He, Y. Su and J. Chen, *ACS Appl. Mater. Interfaces*, 2021, **13**, 52850–52860.

27 A. Zonarsaghar, M. M. Kamazani and S. Z. Ajabshir, *Int. J. Hydrogen Energy*, 2022, **47**, 5403–5417.

28 S. Z. Ajabshir, M. Emsaki and G. Hosseinzadeh, *J. Colloid Interface Sci.*, 2022, **619**, 1–13.

29 S. Z. Ajabshir, S. A. H. Asil and M. S. Niasari, *Sep. Purif. Technol.*, 2021, **267**, 118667–118679.

30 N. K. Chowdhury and B. Bhowmik, *Nanoscale Adv.*, 2021, **3**, 73–93.

31 A. K. Singh and B. Bhowmik, *Nanotechnology*, 2022, **33**, 435501–435511.

32 E. Wongrat, W. Ponhan and S. Choopun, *Ceram. Int.*, 2017, **43**, S520–S524.

33 S. Dutta and A. Dodabalapur, *Sens. Actuators, B*, 2009, **143**, 50–55.

34 C. T. Lee and P. Chou, *IEEE Sens. Lett.*, 2018, **2**, 1–3.

35 B. Chen, H. Liu, X. Li, C. Lu, Y. Ding and B. Lu, *Appl. Surf. Sci.*, 2012, **258**, 1971–1975.

36 P. P. Sahay and R. K. Nath, *Sens. Actuators, B*, 2008, **134**, 654–659.

37 L. Torsi, M. C. Tanese, N. Cioffia, M. C. Gallazzi, L. Sabbatini and P. G. Zambonina, *Sens. Actuators, B*, 2004, **98**, 204–207.

38 H. E. Swanson, H. F. McMurdie, M. C. Morris and E. H. Evans, *Standard X-ray Diffraction Powder Patterns*, 1966, vol. 25, pp. 82–83.

39 S. Z. Ajabshira, M. S. Morassaeib, O. Amiric, M. S. Niasarib and L. K. Foong, *Ceram. Int.*, 2020, **46**, 17186–17196.

40 S. Moshtaghi, S. Z. Ajabshir and M. S. Niasari, *J. Mater. Sci.: Mater. Electron.*, 2016, **27**, 425–435.

41 B. Bhowmik and P. Bhattacharyya, *IEEE Trans. Electron Devices*, 2017, **64**, 2357–2363.

42 S. A. Nasser, *Appl. Surf. Sci.*, 2000, **157**, 14–22.

43 W. Park, J. S. Kim, G. C. Yi, M. H. Bae and H. J. Lee, *Appl. Phys. Lett.*, 2004, **85**, 5052–5054.

44 B. Bhowmik and P. Bhattacharyya, *IEEE Trans. Nanotechnol.*, 2017, **16**, 180–188.

45 A. Bora, K. Mohan, D. Pegu, C. B. Gohain and S. K. Dolui, *Sens. Actuators, B*, 2017, **253**, 977–986.

46 M. T. Vijjapu, S. G. Surya, S. Yuvaraja, X. Zhang, H. N. Alshareef and K. N. Salama, *ACS Sens.*, 2020, **5**, 984–993.

47 A. Hazra, P. P. Chattopadhyay and P. Bhattacharyya, *IEEE Electron Device Lett.*, 2015, **36**, 505–507.

48 T. Ishihara, S. Sato and Y. Takita, *Sens. Actuators, B*, 1996, **30**, 43–45.